

Research paper

Towards better understanding supersonic impact-bonding behavior of cold sprayed 6061-T6 aluminum alloy based on a high-accuracy material model

Qian Wang ^{a,b}, Ninsuh Ma ^{a*}, Xiao-Tao Luo ^{c,*}, Chang-Jiu Li ^c^a Joining and Welding Research Institute, Osaka University, Osaka 567-0047, Japan^b Graduate School of Engineering, Osaka University, Osaka 565-0871, Japan^c State Key Laboratory for Mechanical Behavior of Materials, School of Materials Science and Engineering, Xi'an Jiaotong University, Xi'an, Shaanxi 710049, China

ARTICLE INFO

ABSTRACT

Keywords:
 Cold spray
 Material model
 Dynamic deformation
 Supersonic impact
 Impact bonding

Supersonic impact deformation-induced bonding is at the heart of the cold spray (CS) process, and therein lies the difficulty of clearly understanding CS behaviors. In this study, the supersonic impact-bonding behavior was systematically investigated by accurately reproducing the CS process using a newly developed material model (Ma-Wang material model) with 6061-T6 aluminum alloy (Al6061-T6) as the target material. First, the material properties of the Ma-Wang material model were identified using general flow stress data. Then, the high-fidelity modeling was fully confirmed by comparing the simulated and experimental coefficients of restitution and microparticle deformations over a wide range of impact velocities. More importantly, the rebound origin and bonding features of supersonic impacts between identical and dissimilar materials (Al6061-T6/Al6061-T6 and Al6061-T6/sapphire) were thoroughly explored, revealing that regardless of the substrate type, metallic plastic deformation is the main pathway for energy dissipation (dissipating approximately 90% of the energy). In addition, the rebound of metallic microparticles is highly dependent on the elastic recovery of the substrate. The difference is that during the supersonic impact between dissimilar materials, interfacial friction can be another important pathway for energy dissipation (dissipating approximately 10% of the energy). The coordinated deformation between microparticles and substrate favors supersonic impact-bonding. Further, the distinct features due to jetting and energy can be regarded as precursors to CS bonding.

1. Introduction

Cold spray (CS), a highly anticipated additive manufacturing technology, is explicitly written in the ASTM F2792-12A standard [1,2]. It does not rely on thermal energy, but on the supersonic impact (typically $300\text{--}1200\text{ m}\cdot\text{s}^{-1}$ [3]) of microparticles onto a substrate to form deposits; hence, melting/solidification-related issues (e.g., oxidation, thermal stresses, phase transformation, chemical degradation, and grain growth) can be minimized or eliminated. Minimal oxidation gives CS flexibility and portability, enabling it to be carried out in the open air [4–6]. Low thermal stresses result in low levels of tensile residual stresses, which contribute to the fatigue life of CS products [7–9]. The absence of phase transformation, chemical degradation, and grain growth allows the microstructure and chemical composition of feedstock to be retained in CS products, making CS suitable for depositing a wide variety of materials, including metals and alloys with polycrystalline, nanocrystalline, and amorphous structures [3,10,11], composites using these materials

as matrices [12–14], and even polymers [15] and ceramics [16]. Moreover, CS offers the advantages of high deposition rate and efficiency [7,17,18], 100% reusability of feedstock [19], unrestricted deposition size [5,18–21], and environmental friendliness (because of low temperatures, no dangerous gases or radiations, and no chemically aggressive wastes) [22]. To date, CS has attracted considerable attention from scientific and industrial circles.

Despite the explosive growth of CS research in recent years, the mechanisms governing the interfacial bonding, grain refinement, and residual stress evolution, which determine the final performance of CS products, remain unclear. Taking the example of interfacial bonding, several mechanisms (e.g., mechanical interlocking [23], diffusion [24], interfacial melting [25,26], interfacial amorphization [27], oxide film rupture [28,29], adiabatic shear instability [3,24,30,31], pressure wave spallation [32,33], and vortex-like intermixing [34]) have been successively proposed. There is no unified mechanism yet. However, it is generally accepted that bonding is closely associated with large plastic

* Corresponding authors.

E-mail addresses: ma.ninshu@jwri.osaka-u.ac.jp (N. Ma), luoxiaotao@mail.xjtu.edu.cn (X.-T. Luo).

strains occurring at the interface, manifested as an outward jet (called jetting). Jetting is a vital CS phenomenon, but its formation is highly debated [32,35,36]. The underlying cause is that the nonlinear, nonequilibrium, and ultra-high strain rate (up to 10^8 s^{-1} [3,17,24,30]) responses of materials at the microscopic scale and nanosecond level pose various obstacles to the explicit understanding of supersonic impact-bonding behavior (during CS) either experimentally or by simulation. Recently, the micro-ballistic test platform reported by Hassani et al. [37,38] makes the quantitative in-situ observation of single-particle impact possible, which is helpful for understanding the supersonic impact-bonding behavior. Nevertheless, based on this platform, a detailed assessment of the spatiotemporal evolutions of stress, strain, strain rate, temperature, pressure, energy, and grain size remains challenging, impeding a full understanding of the supersonic impact-bonding behavior. As a result, the quantitative mathematical modeling of CS is imperative.

An accurate material model is essential to quantitative CS modeling. The Johnson-Cook (JC) material model, which has been widely used in CS simulations, suffers from a lack of accuracy at strain rates higher than $10^3\text{--}10^4 \text{ s}^{-1}$ [39–41] and significant temperature rise [42,43]. Several modified JC material models have been proposed in an attempt to solve the accuracy problem of the original model [41,43–46], but the problem has not been eliminated. Alizadeh [44] emphasized that the modified JC material model (with parameters fitted by general flow stress data) is still inadequate for accurately simulating the CS process. To ensure high accuracy, the parameters must be back-optimized based on a series of known particle deformations at different impact velocities, which generate a huge amount of workload virtually and deviate from the original intention of model development. Additionally, the JC material model itself is a purely empirical model, which, together with pure mathematical optimization, may lead to unreliable simulated variables (e.g., stress, strain, strain rate, and temperature), thus discouraging its further extension in CS research. In view of the above, we discarded the JC model structure and developed the Ma-Wang (MW) material model based on dislocation dynamics [47], which achieves the quantified prediction of single-particle impact and is expected to become the cornerstone of future multi-scale or large-scale CS simulations. Cu and Al are among the most commonly used CS materials. In our previous studies [47,48], the high accuracy of the MW material model was fully confirmed against pure Cu.

Herein, 6061-T6 aluminum alloy (Al6061-T6), a representative aluminum alloy, was selected as the target material. The MW model parameters were fitted for Al6061-T6 and applied to CS simulations to validate the accuracy of the model, which is essential to highlight the universality of the MW material model. Additionally, the respective roles of strain hardening, normal-range strain rate hardening, ultra-high strain rate hardening, and thermal softening/hardening of Al6061-T6 in the MW material model were discussed in detail. As we all know, CS is suitable and commonly used for depositing dissimilar materials [2–8, 11–17,20–22,24,25,27–30,34,41]. It is of great importance to fully understand the characteristics of supersonic impact between dissimilar materials, in addition to identical materials. In view of this, sapphire ($\alpha\text{-Al}_2\text{O}_3$) was chosen as a dissimilar material for Al6061-T6 because of its much higher stiffness and good bonding compatibility. Al6061-T6 could be well bonded to sapphire by heteroepitaxy (during CS) [49, 50]. Accordingly, the material deformation and energy conversion were quantitatively analyzed to elucidate the rebound origin and bonding

features during supersonic impact between identical materials (Al6061-T6/Al6061-T6) and dissimilar materials (Al6061-T6/sapphire). An explicit understanding of the supersonic impact-bonding behavior (during CS) of aluminum alloys was provided.

2. Supersonic impact material modeling

In this study, Al6061-T6, a representative aluminum alloy, was selected as the target material. The normal impacts of single Al6061-T6 microparticles on Al6061-T6 substrates and sapphire substrates (Al6061-T6/Al6061-T6 and Al6061-T6/sapphire) were investigated over a wide range of impact velocities (suitable for CS) at room temperature (25 °C in this study). Three-dimensional (3D) modeling is used to facilitate the extraction of various types of energy information and has the potential to be extended to multi-scale and large-scale CS modeling in the future. For both impact systems, the impact processes were simulated using the Lagrangian method in LS-DYNA [26,32,48,51]. The Lagrangian method was utilized for its advantages in tracking moving interfaces, allowing microparticles to be studied separately from substrates, and obtaining detailed energy information about impact, rebound, and even bonding. As a side note, the arbitrary Lagrangian-Eulerian (ALE) [9] and smoothed particle hydrodynamics (SPH) [52] methods have similar advantages but would incur great computational costs for 3D modeling (particularly with large substrate dimensions and fine mesh sizes) in this study. However, they are still being optimized. Considering the effectiveness of the method and the characteristics of this study, the Lagrangian method is preferable.

The geometric dimensions and meshing for all CS simulations are shown in Fig. 1. A quarter axisymmetric geometry was created based on the axisymmetry of the normal impact. The microparticle was set as a sphere with a realistic diameter so that the diameter (d_p) varies in different CS simulations but is basically around 20 μm. For details, see Section 3. The substrate was assumed to be a cylinder with a radius and height of 200 μm, which is large enough to minimize the interference of false waves reflected from the model boundary [53]. For a more detailed explanation, please refer to Supplementary Note S1. Constant stress solid elements (ELFORM = 1) with standard viscous hourglass control were employed to mesh the microparticle and substrate. The whole microparticle and the substrate in the central impact region, as of interest, were divided by a nominal mesh size of 0.5 μm. The substrate in the remaining region was divided into coarse mesh sizes of approximately 10 μm to reduce the computational costs. The corresponding mesh convergence analysis is appended in Supplementary Note S2. The ABCD and ABEF planes were set as symmetric boundaries, and the normal degrees of freedom of the substrate bottom and outer surfaces were constrained to map the substrate to actual macroscopic dimensions. A segment-based pinball contact algorithm, with a coefficient of friction (COF) of 0.2 [26,32,48,51], was invoked to describe the interaction between the microparticle and substrate.

During CS, the metallic material, Al6061-T6, undergoes extreme deformation over a wide range of strain rates (up to 10^8 s^{-1}), with significant temperature increases in localized zones. The self-developed material model, MW material model [47], was adopted to take full account of the coupling effects of strain hardening, normal-range strain rate hardening, ultra-high strain rate hardening, and thermal softening/hardening to accurately reproduce the elastic-plastic response of Al6061-T6. The specific formula is as follows:

$$\sigma = \left\{ [\sigma_{y0} + A(\dot{\varepsilon}^p)^n] + (\alpha\dot{\varepsilon}^p + \beta) \left[1 - \frac{\sigma_{y0} + A(\dot{\varepsilon}^p)^n}{\sigma_{cr}} \right] \ln \left(\frac{\dot{\varepsilon}^p}{\dot{\varepsilon}_s^p} \right) + B \ln \left(\frac{\dot{\varepsilon}^p}{\dot{\varepsilon}_u^p} \right) \right\} \frac{\text{sigmoid} \left(-\frac{T-T_a}{T_m-T_a} b \right)}{\text{sigmoid} \left(-\frac{T_u-T_a}{T_m-T_a} b \right)}^m, \quad (1)$$

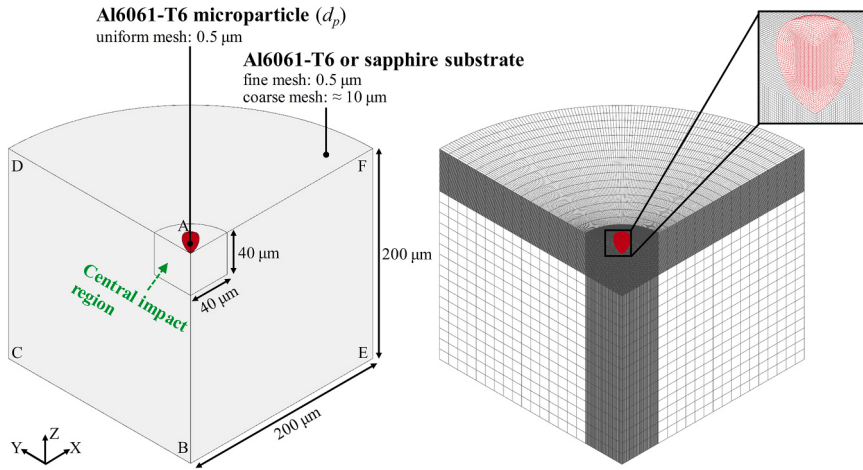


Fig. 1. Geometric dimensions and meshing for both impact systems, Al6061-T6/Al6061-T6 and Al6061-T6/sapphire.

where σ refers to the dynamic flow stress dependent on the transient plastic strain $\dot{\epsilon}^p$, plastic strain rate $\dot{\epsilon}^p$, and temperature T ; σ_{Y0} , A , and n are the parameters that control the MW model strain hardening; $\dot{\epsilon}_u^p$ denotes the reference strain rate (generally 0.001 s^{-1}) for the MW model normal-range strain rate hardening, and α , β , and σ_α are the parameters of this term; $\dot{\epsilon}_u^p$ signifies the minimum strain rate that turns on the phonon-related dislocation drag, and B is the sole parameter of the MW model ultra-high strain rate hardening (notably $B = 0$ when $\dot{\epsilon}^p < \dot{\epsilon}_u^p$); T_R and T_m are the reference temperature (generally 25°C) and the melting point of the metal, respectively; T_a , b , and m are the parameters of the MW model thermal softening/hardening. It is worth noting that in the MW material model, the additional parameter m ($m \leq 1$) coordinates the general thermal softening with the anomalous thermal hardening caused by the phonon-related dislocation drag at ultra-high strain rates [54]. This point is particularly crucial for the high-precision reproduction of low-melting-point CS metals (see Section

3.2 for more details). Alternatively, the JC material model was used for Al6061-T6, as follows:

$$\sigma = \left[A^{JC} + B^{JC}(\dot{\epsilon}^p)^{n^{JC}} \right] \left[1 + C^{JC} \ln \left(\frac{\dot{\epsilon}^p}{\dot{\epsilon}_0^p} \right) \right] \left[1 - \left(\frac{T - T_R}{T_m - T_R} \right)^{m^{JC}} \right], \quad (2)$$

where A^{JC} , B^{JC} , n^{JC} , $\dot{\epsilon}_0^p$, C^{JC} , and m^{JC} are the parameters used in the JC material model. The objective was to make a direct comparison between MW and JC material models. For sapphire, the hypoelastic material model is available because there is hardly any plastic deformation during CS. In addition, all CS simulations are single-particle impacts ending within tens of nanoseconds, which can be viewed as adiabatic processes, as follows:

$$\Delta T = \eta \int_0^{\dot{\epsilon}^p} \frac{\sigma d\dot{\epsilon}^p}{\rho c}, \quad (3)$$

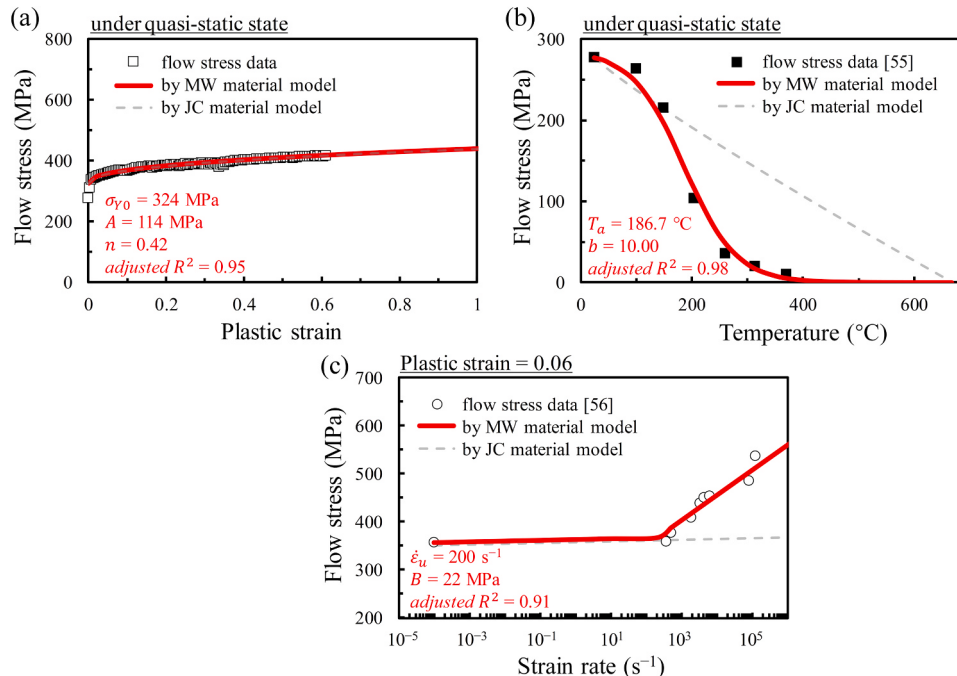


Fig. 2. MW model parameters of Al6061-T6 fitted using general flow stress data: (a) quasi-static flow stress–plastic strain curve, (b) quasi-static flow stress–temperature curve [55], and (c) flow stress–strain rate curve at a constant plastic strain of 0.06 [56]; including a flow stress comparison between MW and JC material models.

where ΔT denotes the temperature increase due to plastic deformation; ρ and c are the density and specific heat of the metal, respectively, η is the fraction of plastic work converted into heat (generally 0.9).

3. Results and discussion

3.1. Determination of model parameters

For Al6061-T6, the MW model parameters were fitted using general flow stress data, as shown in Fig. 2. The plastic strain- and temperature-dependent flow stress curves can be fitted to determine the parameters σ_{y0} , A , and n of the strain hardening portion (Fig. 2(a)), and the parameters T_a and b of the thermal softening/hardening portion (Fig. 2(b)), respectively. The curves obtained under quasi-static conditions are adequate. Because Al6061-T6 belongs to an aluminum series metal and its normal-range strain rate hardening parameters α , β , and σ_{cr} have been reported in our previous study [47], the parameters $\dot{\epsilon}_u^p$ and B of the ultra-high strain rate hardening portion can be confirmed simply by fitting a flow stress-strain rate curve at a constant plastic strain (0.06 in this study), as shown in Fig. 2(c). All the adjusted coefficients of determination (*adjusted R*² values) were higher than 0.9, which indicates that the model is a good fit for the data.

In particular, Fig. 2 includes the flow stress curves plotted by the JC material model, providing a direct comparison of the flow stresses between the MW and JC material models. Both models, with the same strain hardening function, can accurately capture the strain hardening of Al6061-T6, as visualized from the perfectly overlapping flow stress–plastic strain curves (Fig. 2(a)). Nonetheless, the MW material model, using the sigmoid function, reflects the S-shaped thermal softening of Al6061-T6 more closely than the JC material model, which can be seen by comparing the flow stress–temperature curves (Fig. 2(b)). The flow stress–strain rate curves are compared in Fig. 2(c), which clarifies the model consistency for describing the normal-range strain rate hardening

of Al6061-T6 ($< 10^3 \text{ s}^{-1}$), as well as the high accuracy of the MW material model with respect to ultra-high strain rate hardening ($\geq 10^3 \text{ s}^{-1}$). Please note that we do not intend to offend the JC material model but rather highly endorse it as one of the most widely applied material models for large deformation problems. The MW material model is expected to be similar, with fewer model parameters, easy to fit using general flow stress data, and easy to integrate into simulation codes. It is therefore taken as a benchmark to highlight the characteristics of the MW material model and to better understand the supersonic impact-bonding behavior during CS. All parameters of Al6061-T6 used in the MW and JC material models, as well as the sapphire used in the hypoelastic material model, are listed in Table 1.

3.2. Reproduction of supersonic impact behavior

To identify the accuracy of Al6061-T6 during CS, the MW material model was applied to simulate a single Al6061-T6 microparticle impacting a sapphire substrate over a wide range of impact velocities. Specifically, the ability to accurately reproduce the energy dissipation and overall deformations of the Al6061-T6 microparticles was examined, as shown in Fig. 3 and Fig. 4. The coefficient of restitution (COR), which can be defined as the ratio of the rebound velocity (V_r) to the impact velocity (V_i), is typically introduced to characterize the energy dissipation in impact events. Fig. 3 provides a systematic comparison of the simulated and experimental CORs over a wide range of impact velocities. Overall, the simulated CORs based on the MW and JC material models are in good agreement with the experimental results, demonstrating 99% energy dissipation of Al6061-T6 microparticles at impacts above the speed of sound in air. The JC-simulated CORs deviate from the experimental ones only when the impact velocities are higher than $600 \text{ m}\cdot\text{s}^{-1}$. Consequently, the energy dissipation of the Al6061-T6 microparticles can be correctly reproduced by both material models; however, the accuracy of the MW material model is higher than that of the JC material model.

Fig. 4 compares the overall deformations of Al6061-T6 microparticles simulated based on the MW and JC material models with the experimental results over a wide range of impact velocities. Note that the deformation of the sapphire substrate is not detailed because it has almost no deformation. The red and blue dotted outlines are used to mark the MW- and JC-simulated particle deformations. At impact velocities below the speed of sound in air, the MW- and JC-simulated particle deformations are almost identical and agree well with the experimental ones, as shown in Fig. 4(a), (b), (g), (h), (m), and (n). However, both of them are significantly different when V_i exceeds the

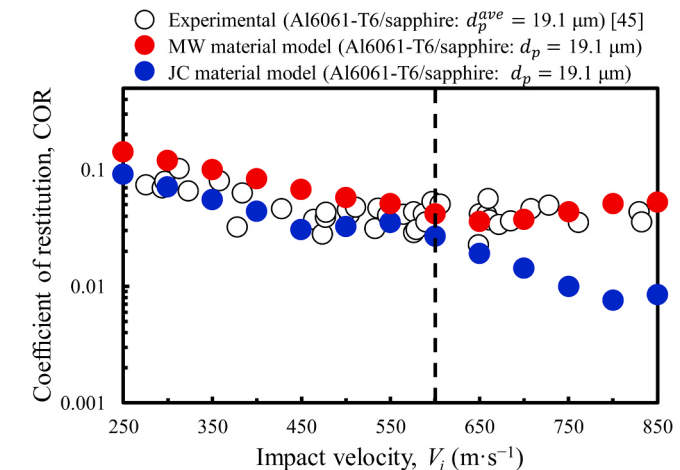


Fig. 3. Comparison of the CORs for Al6061-T6/sapphire impact system from subsonic to supersonic regimes, obtained experimentally [45] and from simulations based on the MW and JC material models.

Table 1

All parameters of Al6061-T6 used in the MW and JC material models, as well as sapphire used in the hypoelastic material model.

(Al6061-T6)		(sapphire)	
MW model	JC model [26]	Hypoelastic model [45]	
Parameters	Parameters	Parameters	
Young's modulus E (GPa)	68.9	E (GPa)	68.9
Poisson's ratio ν	0.33	ν	0.33
ρ (kg·m ⁻³)	2703	ρ (kg·m ⁻³)	2703
c (J·kg ⁻¹ ·°C ⁻¹)	875	c (J·kg ⁻¹ ·°C ⁻¹)	875
η	0.9	η	0.9
σ_{y0} (MPa)	324	A^{JC} (MPa)	324
A (MPa)	114	B^{JC} (MPa)	114
n	0.42	n^{JC}	0.42
$\dot{\epsilon}_s^p$ (s ⁻¹)	0.001	$\dot{\epsilon}_0^p$ (s ⁻¹)	1
α (MPa)	4.52	C^{JC}	0.002
β (MPa)	0.65	–	–
σ_{cr} (GPa)	1.5	–	–
$\dot{\epsilon}_u^p$ (s ⁻¹)	200	–	–
B (MPa)	22	–	–
T_R (°C)	25	T_R (°C)	25
T_m (°C)	652	T_m (°C)	652
T_a (°C)	186.7	m^{JC}	1.34
b	10.00	–	–
m	0.05	–	–

Note: m is the only parameter to be back-optimized (see Section 3.2 for more details).

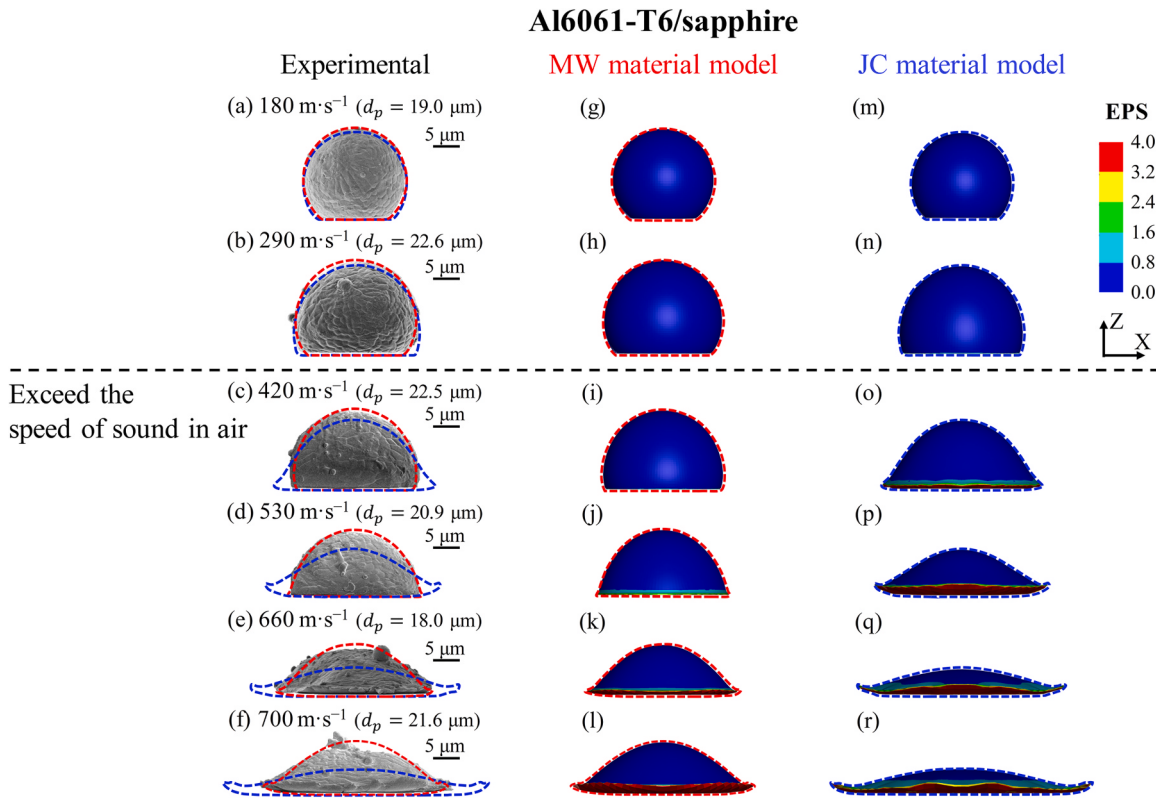


Fig. 4. Comparison of the particle deformations for Al6061-T6/sapphire impact system from subsonic to supersonic regimes, obtained (a–f) experimentally [45] and from simulations based on the (g–l) MW and (m–r) JC material models. The MW- and JC-simulated particle deformations are marked with red and blue dotted outlines, respectively. EPS refers to the effective plastic strain.

speed of sound in air. The MW-simulated particle deformation is still highly consistent with the experimental one, whereas the deviation between the JC-simulated and experimental particle deformations becomes more pronounced with the increase of V_i , as shown in Fig. 4(c–f), (i–l), and (o–r). The main reason for the deviation is that the JC material model fails to accurately capture the effects of strain rate higher than 10^3 s⁻¹ and temperature, as visualized in Fig. 2. Therefore, compared to the JC material model, the MW material model accurately reproduces the overall deformations of Al6061-T6 microparticles from subsonic to supersonic regimes. Meanwhile, direct evidence that the JC material

model is not applicable for an accurate description of material deformation under supersonic impact emphasizes the need to develop a proprietary material model for CS.

It is important to note that the MW material model uses a back-optimized parameter m . This is because, for some metals, including Al and its alloys [54,57,58], the temperature has an anomalous hardening effect on the flow stress caused by the phonon-related dislocation drag at ultra-high strain rates. Ideally, a specialized formula is needed to describe the anomalous thermal hardening at ultra-high strain rates. However, anomalous thermal hardening is difficult to formulate owing to the lack of systematic temperature-dependent data at ultra-high strain rates. Thermal hardening and softening are similar in that their effects are absent at T_R and become very significant near T_m . To simplify the material modeling, parameter m is used to consider them in an integrated manner (Eq. (1)). A comparison of Fig. 5 and Fig. 4(e) evidences that the anomalous thermal hardening cannot be ignored for Al6061-T6 during CS. The m value was back-optimized to 0.05 (Table 1) according to the known deformation in Fig. 4(e), which ensures the high accuracy of the MW material model for simulating Al6061-T6 deformation over a wide range of impact velocities, as shown in Fig. 4(a–l) and Section 3.4.2.

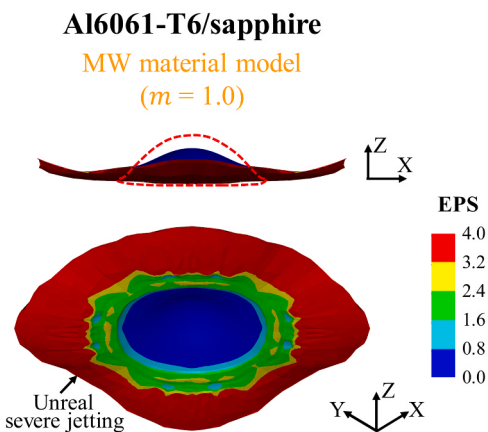


Fig. 5. Assumed deformation of the Al6061-T6 microparticle ($d_p = 18.0 \mu\text{m}$) at a V_i of $660 \text{ m}\cdot\text{s}^{-1}$ for Al6061-T6/sapphire impact system, based on the MW material model without thermal hardening (i.e., $m = 1$). The experimental deformation is shown in Fig. 4(e), and the simulated deformation in Fig. 4(k) is marked with the red dotted outline.

3.3. Individual effects of strain, strain rate, and temperature

All the aforementioned comparisons of Al6061-T6 provide favorable evidence to demonstrate the high accuracy of the MW material model. Moreover, the systematic validation against Al6061-T6, following the validation against pure Cu [47,48], highlights the model universality and makes it possible to understand the CS process explicitly. During CS, metallic materials suffer strain hardening, normal-range strain rate hardening, ultra-high strain rate hardening, and thermal softening/hardening, all of which are considered in the MW material model

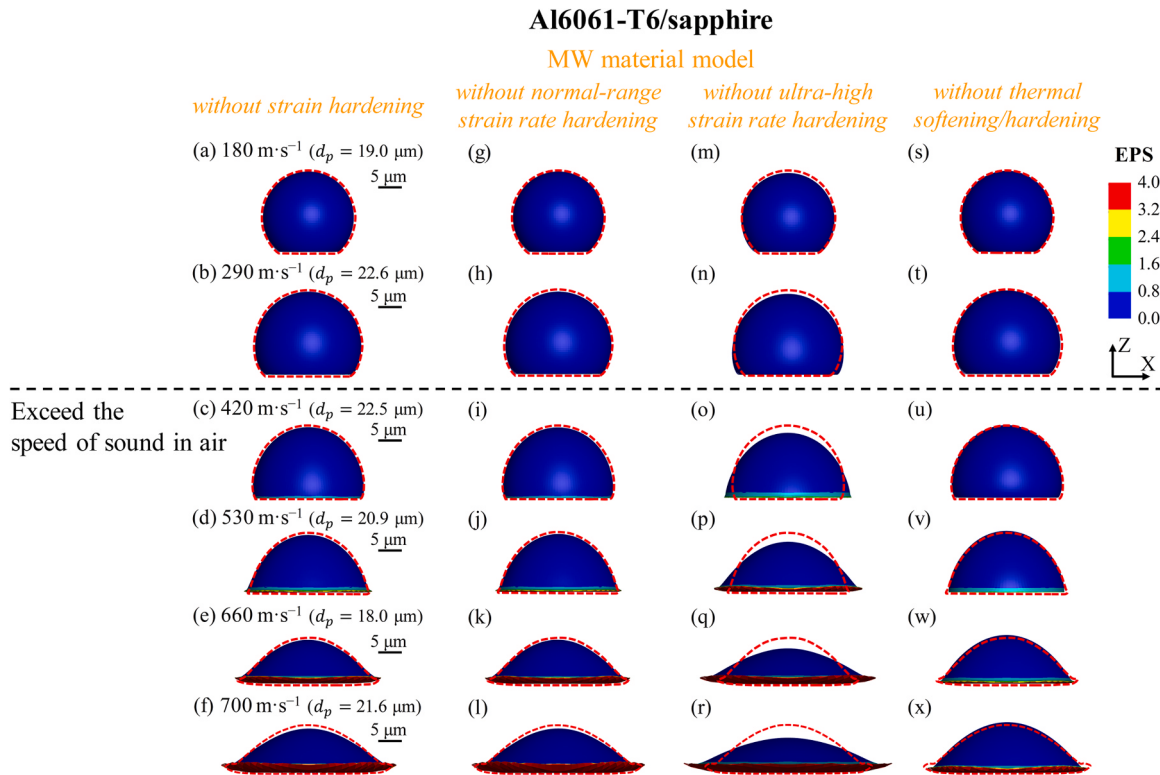


Fig. 6. Assumed deformations of Al6061-T6 microparticles for Al6061-T6/sapphire impact system from subsonic to supersonic regimes, based on the MW material models without individual terms: (a–f) strain hardening, (g–l) normal-range strain rate hardening, (m–r) ultra-high strain rate hardening, and (s–x) thermal softening/hardening. The experimental deformations are shown in Fig. 4(a–f), and the simulated deformations in Fig. 4(g–l) are marked with the red dotted outlines.

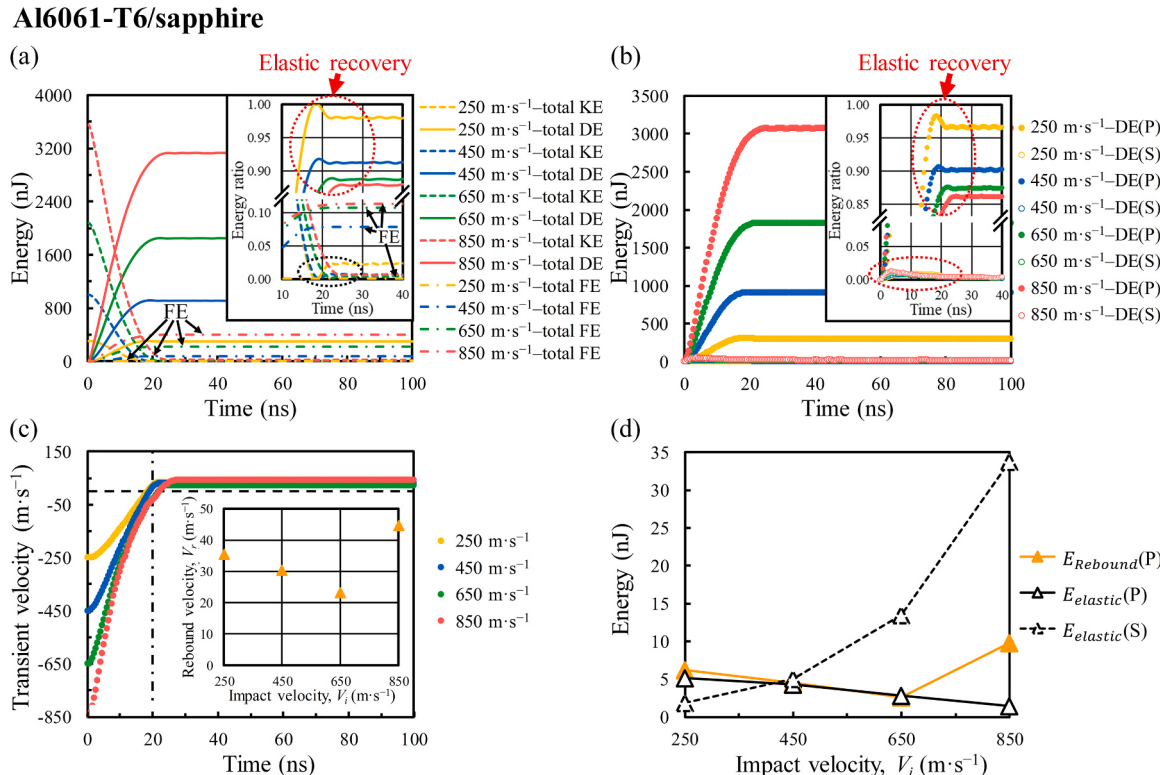


Fig. 7. (a) Overall energy conversion for Al6061-T6/sapphire impact system, (b) individual DEs, and (c) transient particle velocity at four impact velocities of 250, 450, 650, and 850 $\text{m}\cdot\text{s}^{-1}$. (d) Comparison of individual E_{elastic} and $E_{\text{Rebound}}(\text{P})$. These data were extracted from the simulations based on the MW material model in Fig. 3. KE , FE , DE , E_{elastic} , and E_{Rebound} represent kinetic energy, friction energy, deformation energy, and rebound energy, respectively. (P) and (S) refer to the microparticle and the substrate, respectively. Energy ratio indicates the proportion of corresponding energy in the total energy.

(Eq. (1)). To better understand their respective effects, we further applied the MW material models without individual terms to simulate a single Al6061-T6 microparticle impacting a sapphire substrate over a wide range of impact velocities. The corresponding assumed deformations of the Al6061-T6 microparticles are shown in Fig. 6. The assumed deformations, corresponding to the experimental deformations in Fig. 4(a-f), are comparable to the simulated deformations in Fig. 4(g-l).

First, the respective effects of strain hardening and normal-range strain rate hardening can be discussed by comparing Fig. 6(a-f) and Fig. 6(g-l) with Fig. 4(g-l), respectively. Clearly, both have little effect on the particle deformation. Second, a comparison of Fig. 6(m-r) and Fig. 4(g-l) shows that the MW material model without ultra-high strain rate hardening, similar to the JC material model (Fig. 4(m-r)), can grossly overestimate the particle deformation, clarifying the significant effect of ultra-high strain rate hardening. Nonetheless, this model still has higher accuracy than the JC material model, largely depending on the more physical model structure. Third, the assumed deformations in Fig. 6(s-x) are slightly smaller than the simulated deformations in Fig. 4(g-l), indicating that thermal softening/hardening has a very weak effect on particle deformation. This weak temperature effect can be attributed to the balance between the general thermal softening (Fig. 2(b)) and the anomalous thermal hardening caused by the phonon-related dislocation drag at ultra-high strain rates (Fig. 5). Consequently, their respective effects on particle deformation become stronger with increasing V_i owing to the increasing strain, strain rate, and temperature. However, in any case, ultra-high strain rate hardening plays a key role in Al6061 deformation during CS. This finding is consistent with that of our previous study on pure Cu [47] and Ref. [32], which supports the idea that ultra-high strain rate hardening rather than temperature softening/hardening (i.e., the effect of adiabatic temperature rise) predominates the CS deformation behavior of metallic materials.

3.4. Capturing rebound origin and bonding features

3.4.1. Al6061-T6/sapphire

In the Al6061-T6/sapphire impact system, the Al6061-T6 microparticles invariably rebound after impact, despite the tremendous energy dissipation involved in the process (Fig. 3). To better understand the causes of particle rebound, the energy conversion over a wide range of impact velocities was investigated in detail. Fig. 7 shows the detailed energy information at four impact velocities of 250, 450, 650, and 850 m·s⁻¹, which were extracted from the simulations based on the MW material model in Fig. 3. To exclude the effects of size difference and ensure comparability, all the microparticles were 19.1 μm in diameter. The overall energy conversions in Fig. 7(a) illustrate the impact process, that is, the conversion of kinetic energy (KE) into deformation energy (DE). The DE consists of plastic DE ($E_{plastic}$, dissipated in the form of heat generation, microstructure evolution, etc.) and elastic DE ($E_{elastic}$, converted back to KE). At approximately 20 ns, a sudden decrease in the DE curves and a sudden increase in the KE curves signify the release of $E_{elastic}$ (inset of Fig. 7(a)). Simultaneously, the microparticles start to rebound (Fig. 7(c)), which indicates that the elastic recovery is the root cause of particle rebound. The individual DEs of the microparticle and the substrate (DE(P) and DE(S)) in Fig. 7(b) show that both underwent elastic recovery. To clarify their respective roles in particle rebound, the individual $E_{elastic}$ values of the microparticles and substrates ($E_{elastic}(P)$ and $E_{elastic}(S)$) were compared with the rebound energy of the microparticles ($E_{Rebound}(P)$), as shown in Fig. 7(d). At a V_i of 250 m·s⁻¹, the almost zero $E_{elastic}(S)$ means that the particle rebound is mainly triggered by the elastic recovery of the microparticle. However, as V_i increases, the $E_{elastic}(S)$ steeply increases, while $E_{elastic}(P)$ gradually decreases or approaches zero, indicating that the elastic recovery of the substrate gradually regulates the particle rebound. In summary, in the Al6061-T6/sapphire impact system, the particle rebound originates from the elastic recovery of the microparticle and the substrate, and either of them plays

a leading role depending on V_i .

More information can be obtained from Fig. 7. First, KE is converted into friction energy (FE), in addition to DE. Fig. 7(a) shows that FE increases significantly with V_i , which implies that the energy dissipated by interfacial friction during supersonic impact is not negligible. Second, DE is the sum of DE(P) and DE(S). Fig. 7(b) specifies that the DE converted from KE is used almost exclusively for particle deformation, such that $DE \approx DE(P)$. The DE(S) is close to zero regardless of V_i , illustrating the difficulty of deforming the sapphire substrate in the Al6061-T6/sapphire impact system. The near-zero substrate deformation is one of the key reasons that interface bonding cannot be formed in this impact system. Third, the particle rebound is determined by the elastic recovery. $E_{elastic}$ is expressed as follows:

$$E_{elastic} = \int \frac{1}{2} \frac{\sigma^2}{E} dV, \quad (4)$$

where dV is the volume differential. As incompressible materials, Al6061-T6 and sapphire exhibit almost zero volume change, resulting in extremely low $E_{elastic}(P)$ and $E_{elastic}(S)$, as shown in Fig. 7(a), (b), and (d). Accordingly, $E_{Rebound}(P)$ accounts for only 1% of the total energy during supersonic impact, as shown in Fig. 7(c) and (d) and Fig. 3. Incidentally, V_r decreases first and then increases with increasing V_i (inset of Fig. 7(c)), which has also been found experimentally [45], most likely because of the transition of the leading role of particle rebound (Fig. 7(d)). A clearer interpretation is left for future research.

Our previous study [48] showed that for the Cu/Cu impact system, the energy dissipated by interfacial friction during supersonic impact is negligible. This view is the exact opposite of that shown in Fig. 7. To elucidate the formation of the obvious FEs in Fig. 7, the evolutions of pressure, effective strain rate (ESR), and horizontal velocity were discussed in detail, for example, at a V_i of 650 m·s⁻¹, as shown in Fig. 8. Similar to the previous study, the supersonic impact generates high pressures near the interface, which in turn causes great pressure gradients. The material near the interface accelerates horizontally outward under the action of pressure gradients. Because the free-surface pressure is known to be zero, the pressure gradient near the interface edge is the largest, resulting in the highest ESR and thus the highest horizontal velocity. The above phenomena support the principle that pressure release drives material deformation during CS. Nevertheless, it is worth noting that the particle and the substrate have significantly different pressures generated by the supersonic impact owing to their dissimilar materials, which in turn cause significant differences in pressure gradients, ESRs, and horizontal velocities. Consequently, the obvious FE can be attributed to the significant relative motion between the microparticle and the substrate at the interface. It is suggested that interfacial friction is another important energy dissipation pathway in addition to plastic deformation during supersonic impact between dissimilar materials. Further evidence is provided in Section 3.4.2.

3.4.2. Al6061-T6/Al6061-T6

The supersonic impact between metallic materials (particularly identical metals) has been widely welcomed by CS, among which impact-induced bonding is the top priority of CS research. Moreover, a direct comparison is imperative to explicitly identify the similarities and differences in supersonic impacts between identical and dissimilar materials. For these reasons, we specifically investigated the impact system of a single Al6061-T6 microparticle impacting an Al6061-T6 substrate by combining numerical simulations and experimental validation.

Fig. 9 shows the overall deformation of the Al6061-T6/Al6061-T6 impact system obtained experimentally and from simulations based on the MW and JC material models. The substrate is deformed along with the microparticle. The MW- and JC-simulated deformation profiles are marked with purple and green dotted outlines, respectively. By comparing Fig. 9(a-d) and Fig. 9(e-h), it can be seen visually that the MW-simulated particle deformation and penetration depth are in good

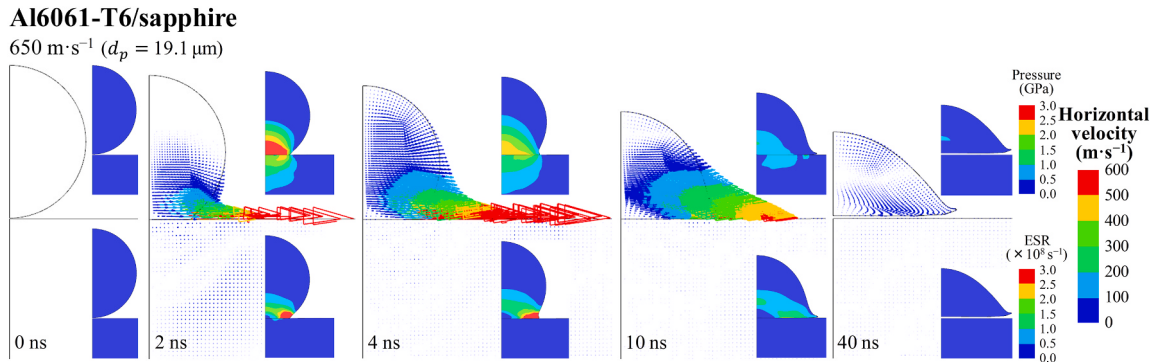


Fig. 8. Evolutions of pressure, effective strain rate (ESR), and horizontal velocity for Al6061-T6/sapphire impact system at an V_i of $650 \text{ m}\cdot\text{s}^{-1}$. These data were extracted from the simulations based on the MW material model in Fig. 3. The arrow represents the horizontal velocity, and its color and size can indicate the velocity magnitude.

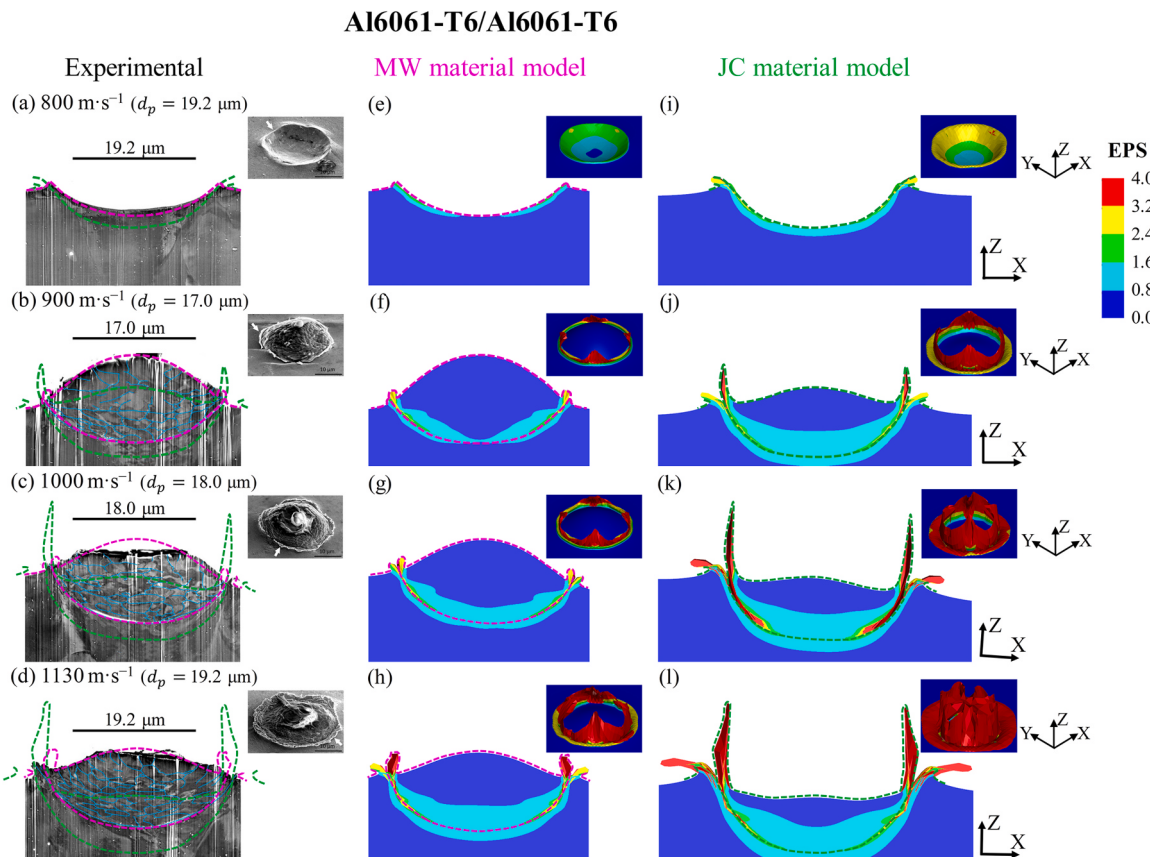


Fig. 9. Comparison of the overall deformations for Al6061-T6/Al6061-T6 impact system after supersonic impacts at 800, 900, 1000, and $1130 \text{ m}\cdot\text{s}^{-1}$, obtained (a–d) experimentally [45] and from simulations based on the (e–h) MW and (i–l) JC material models. The MW- and JC-simulated deformation profiles are marked with purple and green dotted outlines, respectively.

agreement with the experimental ones at different supersonic impact velocities. In particular, with the application of the MW material model, the jetting phenomena occurring at impact velocities higher than the critical bonding velocity (V_{cr}) of $840 \pm 10 \text{ m}\cdot\text{s}^{-1}$ can also be reproduced appropriately. As expected, the JC material model overestimates the particle deformations, penetration depths, and even the jetting phenomena at the interface edges, as shown in Fig. 9(i–l). Consequently, the MW material model has an overwhelming advantage over the JC material model for describing material deformation in the Al6061-T6/Al6061-T6 impact system under supersonic impact. The above evidence further corroborates the high accuracy of the MW material model.

Incidentally, the MW-simulated results indicate that adiabatic shear instability is not necessary for jet formation (see Supplementary Note S3).

Based on the MW material model, the energy conversion of the Al6061/Al6061 impact system is discussed in detail, as shown in Fig. 10. An FE close to zero can be neglected, independent of V_i (Fig. 10(a)). Almost all the KE is converted to DE, of which 95% is dissipated through plastic deformation and less than 5% is released through elastic recovery (Fig. 10(b)). The elastic recovery of the substrate in particular triggers the particle rebound (Fig. 10(b–d)). $E_{\text{elastic}}(S)$ increases with V_i , and correspondingly, V_r and $E_{\text{Rebound}}(P)$ also increase with V_i (Fig. 10(c) and

Al6061-T6/Al6061-T6

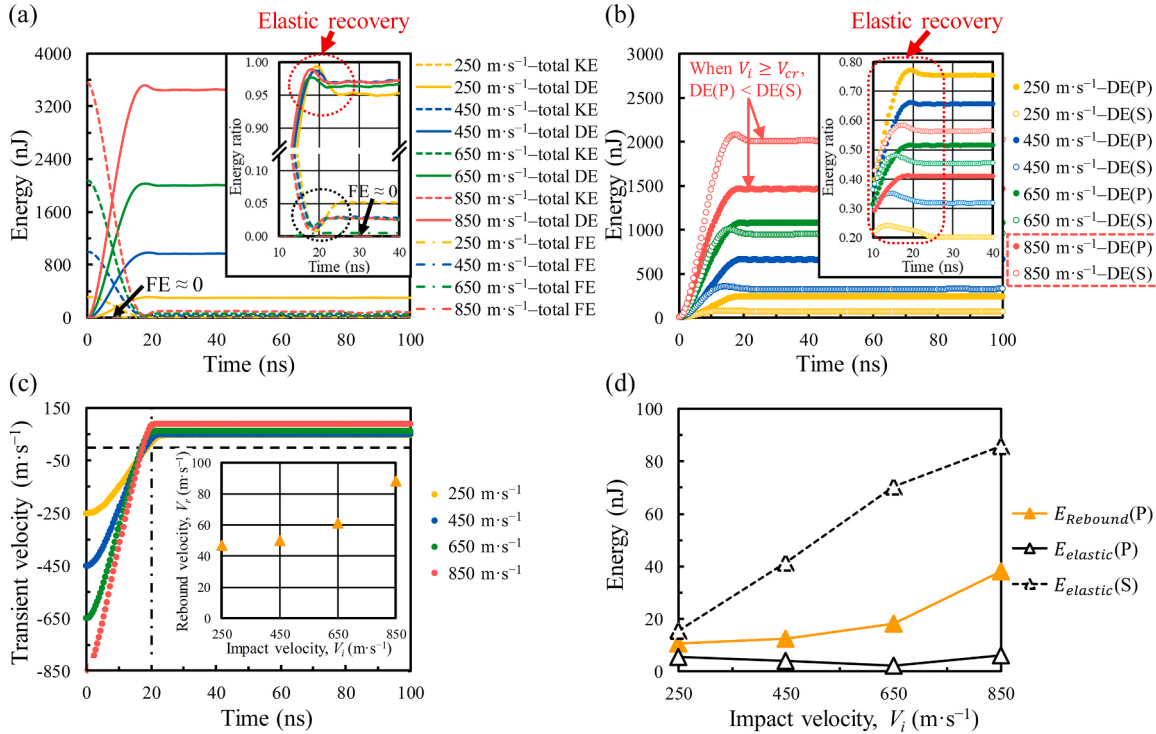


Fig. 10. (a) Overall energy conversion for Al6061-T6/Al6061-T6 impact system, (b) individual DEs, and (c) transient particle velocity at four impact velocities of 250, 450, 650, and 850 m·s⁻¹. (d) Comparison of individual $E_{elastic}$ and $E_{Rebound}(P)$. The diameter of all Al6061-T6 microparticles is 19.1 μm . A direct comparison of this figure with Fig. 7 explicitly identifies the similarities and differences in supersonic impacts between identical and dissimilar materials.

(d)). Both DE(P) and DE(S) increase with V_i . Nevertheless, DE(S) is much lower than DE(P) impacted at a V_i of 250 m·s⁻¹, and gradually approaches DE(P) as V_i increases, even higher than DE(P) at a V_i of 850 m·s⁻¹ just above V_{cr} (Fig. 10(b)). A direct comparison of the above results with those in Fig. 7 explicitly identifies the similarities and differences in supersonic impacts between identical and dissimilar materials. There are three similarities. First, KE is mainly converted to DE, of which very little can be released through elastic recovery. Second, the particle rebound originates from elastic recovery and depends more on the elastic recovery of the substrate than on that of the microparticle during supersonic impact. Third, both systems support $DE(P) < DE(S)$ as a bonding feature, emphasizing that coordinated particle-substrate deformation is preferred for CS bonding. The notable difference is whether the FE can be negligible during supersonic impact. Supplementary Note S4 provides further support for the notable difference.

FE is negligible during supersonic impact between identical mate-

rials (Fig. 10) but should be taken seriously during supersonic impact between dissimilar materials (Fig. 7). Fig. 11 displays the evolutions of pressure, ESR, and horizontal velocity for the Al6061-T6/Al6061-T6 impact system at a V_i of 650 m·s⁻¹, which still support the principle that pressure release drives material deformation during supersonic impact. A direct comparison of Fig. 11 with Fig. 8 provides a better understanding of the FE difference between the two impact systems. The horizontal velocities of the microparticle and the substrate during supersonic impact between identical materials are almost the same (Fig. 11); therefore, the FE can be neglected. In contrast, during the supersonic impact between dissimilar materials, the horizontal velocity of the microparticle differs dramatically from that of the substrate (Fig. 8), and accordingly, the FE is obvious and should be noted. This comparison emphasizes that interfacial friction is another important energy dissipation pathway besides plastic deformation during supersonic impact between dissimilar materials.

Al6061-T6/Al6061-T6

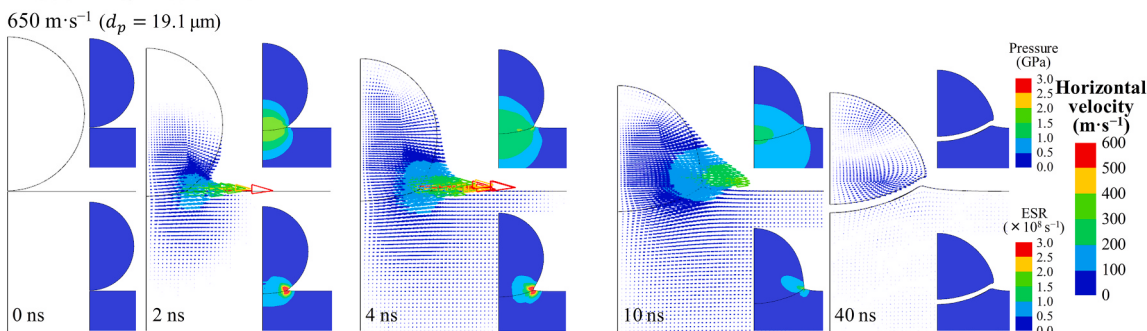


Fig. 11. Evolutions of pressure, ESR, and horizontal velocity for Al6061-T6/Al6061-T6 impact system at an V_i of 650 m·s⁻¹. The diameter of the Al6061-T6 microparticle is 19.1 μm . A direct comparison of this figure with Fig. 8 provides a better understanding of the FE difference between the two impact systems.

Finally, some remarks about the MW material model are presented. Although the MW material model was developed specifically for CS, it has the potential to be applied to other supersonic impact-related fields, such as laser shock peening [59], high-speed machining [60], explosive welding [32,61], and shaped charge [32,62]. In particular, laser shock peening is currently advancing the application of the MW material model in this field. However, the MW material model has limitations. First, it was developed based on the dislocation dynamics of metals and is therefore only applicable to metals (as evidenced in this study and Refs. [47,48]) and not polymers or ceramics. Second, it only considers the material response for strain rates of 10^{-3} – 10^9 s $^{-1}$ (as evidenced in this study and Refs. [47,48]); therefore, it is uncertain whether it is valid beyond that strain rate range.

4. Conclusions

The MW material model enables quantitative analysis of the material deformation as well as the energy conversion of both Al6061/sapphire and Al6061/Al6061 impact systems over a wide range of impact velocities. This study provides an explicit understanding of supersonic impact-bonding behavior (during CS) of aluminum alloys. The conclusions are as follows:

- (1) In the MW material model, all parameters except m of Al6061-T6 were determined by fitting the general flow stress data. The m value was back-optimized with only one known particle deformation. The high accuracy of this model was fully validated for impact systems in both subsonic and supersonic regimes.
- (2) The individual effects of the MW material model on Al6061-T6 deformation were quantified to explicitly clarify that ultra-high strain rate hardening rather than temperature softening/hardening (i.e., the effect of adiabatic temperature rise) predominates the CS deformation behavior of metallic materials.
- (3) In both impact systems, most of the KE is dissipated through plastic deformation, while a very small amount is released through elastic recovery to trigger particle rebound. Moreover, both systems support $DE(P) < DE(S)$ as a bonding feature, emphasizing that coordinated particle-substrate deformation is favorable for supersonic impact-bonding.
- (4) Notably, interfacial friction is another important energy dissipation pathway in addition to plastic deformation during supersonic impact between dissimilar materials.

CRediT authorship contribution statement

Qian Wang: Conceptualization, Methodology, Software, Data curation, Writing - original draft, Writing - review & editing. **Ninshu Ma:** Supervision, Resources, Methodology, Data curation, Writing - review & editing. **Xiao-Tao Luo:** Resources, Writing - review & editing. **Chang-Jiu Li:** Resources.

Declaration of Competing Interest

The authors declare that they have no known competing financial interests or personal relationships that could have appeared to influence the work reported in this paper.

Acknowledgments

This research was partially supported by the Japan Society for the Promotion of Science (Grants-in-Aid for Scientific Research: 20H02452) and Project to Create Research and Educational Hubs for Innovative Manufacturing in Asia (JWRI, Osaka University).

Appendix A. Supporting information

Supplementary data associated with this article can be found in the online version at doi:10.1016/j.addma.2021.102469.

References

- [1] J.M. Flynn, A. Shokrani, S.T. Newman, V. Dhokia, Hybrid additive and subtractive machine tools—Research and industrial developments, *Int. J. Mach. Tools Manuf.* 101 (2016) 79–101.
- [2] W. Li, K. Yang, S. Yin, X. Yang, Y. Xu, R. Lupoi, Solid-state additive manufacturing and repairing by cold spraying: a review, *J. Mater. Sci. Technol.* 34 (2018) 440–457.
- [3] A. Moridi, S.M. Hassani-Gangaraj, M. Guagliano, M. Dao, Cold spray coating: review of material systems and future perspectives, *Surf. Eng.* 30 (2014) 369–395.
- [4] J.G. Lee, D.Y. Kim, B. Kang, D. Kim, H.E. Song, J. Kim, W. Jung, D. Lee, S.S. Al-Deyab, S.C. James, S.S. Yoon, Nickel–copper hybrid electrodes self-adhered onto a silicon wafer by supersonic cold-spray, *Acta Mater.* 93 (2015) 156–163.
- [5] S. Yin, P. Cavaliere, B. Aldwell, R. Jenkins, H. Liao, W. Li, R. Lupoi, Cold spray additive manufacturing and repair: fundamentals and applications, *Addit. Manuf.* 21 (2018) 628–650.
- [6] X.T. Luo, Y. Ge, Y. Xie, Y. Wei, R. Huang, N. Ma, C.S. Ramachandran, C.J. Li, Dynamic evolution of oxide scale on the surfaces of feed stock particles from cracking and segmenting to peel-off while cold spraying copper powder having a high oxygen content, *J. Mater. Sci. Technol.* 67 (2021) 105–115.
- [7] S. Bagherifard, S. Monti, M.V. Zuccoli, M. Riccio, J. Kondás, M. Guagliano, Cold spray deposition for additive manufacturing of freeform structural components compared to selective laser melting, *Mater. Sci. Eng. A-Struct. Mater. Prop. Microstruct. Process.* 721 (2018) 339–350.
- [8] C.M. Sample, V.K. Champagne, A.T. Nardi, D.A. Lados, Factors governing static properties and fatigue, fatigue crack growth, and fracture mechanisms in cold spray alloys and coatings/repairs: a review, *Addit. Manuf.* 36 (2020), 101371.
- [9] Q. Wang, X. Luo, S. Tsutsumi, T. Sasaki, C. Li, N. Ma, Measurement and analysis of cold spray residual stress using arbitrary Lagrangian–Eulerian method, *Addit. Manuf.* 35 (2020), 101296.
- [10] P.S. Phani, V. Vishnukanthan, G. Sundararajan, Effect of heat treatment on properties of cold sprayed nanocrystalline copper alumina coatings, *Acta Mater.* (2007) 4741–4751.
- [11] D. Lahiri, P.K. Gill, S. Scudino, C. Zhang, V. Singh, J. Karthikeyan, N. Munroe, S. Seal, A. Agarwal, Cold sprayed aluminum based glassy coating: synthesis, wear and corrosion properties, *Surf. Coat. Technol.* 232 (2013) 33–40.
- [12] D.J. Woo, F.C. Heer, L.N. Brewer, J.P. Hooper, S. Osswald, Synthesis of nanodiamond-reinforced aluminum metal matrix composites using cold-spray deposition, *Carbon* 86 (2015) 15–25.
- [13] X. Xie, Z. Tan, C. Chen, Y. Xie, H. Wu, X. Yan, S. Gao, Z. Li, G. Ji, H. Liao, Synthesis of carbon nanotube reinforced Al matrix composite coatings via cold spray deposition, *Surf. Coat. Technol.* 405 (2021), 126676.
- [14] C. Chen, Y. Xie, X. Yan, M. Ahmed, R. Lupoi, J. Wang, Z. Ren, H. Liao, S. Yin, Tribological properties of Al/diamond composites produced by cold spray additive manufacturing, *Addit. Manuf.* 36 (2020), 101434.
- [15] K. Ravi, W.L. Sulen, C. Bernard, Y. Ichikawa, K. Ogawa, Fabrication of micro-/nano-structured super-hydrophobic fluorinated polymer coatings by cold-spray, *Surf. Coat. Technol.* 373 (2019) 17–24.
- [16] J.H. Lee, H.L. Jang, K.M. Lee, H.R. Baek, K. Jin, K.S. Hong, J.H. Noh, H.K. Lee, In vitro and in vivo evaluation of the bioactivity of hydroxyapatite-coated polyetheretherketone biocomposites created by cold spray technology, *Acta Biomater.* 9 (2013) 6177–6187.
- [17] X.T. Luo, C.X. Li, F.L. Shang, G.J. Yang, Y.Y. Wang, C.J. Li, High velocity impact induced microstructure evolution during deposition of cold spray coatings: a review, *Surf. Coat. Technol.* 254 (2014) 11–20.
- [18] H. Wu, X. Xie, M. Liu, C. Chen, H. Liao, Y. Zhang, S. Deng, A new approach to simulate coating thickness in cold spray, *Surf. Coat. Technol.* 382 (2020), 125151.
- [19] J. Perry, P. Richer, B. Jodoin, E. Matte, Pin fin array heat sinks by cold spray additive manufacturing: economics of powder recycling, *J. Therm. Spray. Technol.* 28 (2019) 144–160.
- [20] R.N. Raoelison, C. Verdy, H. Liao, Cold gas dynamic spray additive manufacturing today: deposit possibilities, technological solutions and viable applications, *Mater. Des.* 133 (2017) 266–287.
- [21] H. Wu, X. Xie, M. Liu, C. Verdy, Y. Zhang, H. Liao, S. Deng, Stable layer-building strategy to enhance cold-spray-based additive manufacturing, *Addit. Manuf.* 35 (2020), 101356.
- [22] J. Villafuerte, Modern Cold Spray: Materials, Process, and Applications, Springer, Switzerland, 2015.
- [23] R. Morgan, P. Fox, J. Pattison, C. Sutcliffe, W. O'Neill, Analysis of cold gas dynamically sprayed aluminium deposits, *Mater. Lett.* 58 (2004) 1317–1320.
- [24] T. Schmidt, F. Gärtner, H. Assadi, H. Kreye, Development of a generalized parameter window for cold spray deposition, *Acta Mater.* 54 (2006) 729–742.
- [25] G. Bae, S. Kumar, S. Yoon, K. Kang, H. Na, H.J. Kim, C. Lee, Bonding features and associated mechanisms in kinetic sprayed titanium coatings, *Acta Mater.* 57 (2009) 5654–5666.
- [26] X. Wang, F. Feng, M.A. Klecka, M.D. Mordasky, J.K. Garofano, T. El-Wardany, A. Nardi, V.K. Champagne, Characterization and modeling of the bonding process in cold spray additive manufacturing, *Addit. Manuf.* 8 (2015) 149–162.

- [27] K.H. Ko, J.O. Choi, H. Lee, The interfacial restructuring to amorphous: a new adhesion mechanism of cold-sprayed coatings, *Mater. Lett.* 175 (2016) 13–15.
- [28] Y. Xie, S. Yin, C. Chen, M.P. Planche, H. Liao, R. Lupoi, New insights into the coating/substrate interfacial bonding mechanism in cold spray, *Scr. Mater.* 125 (2016) 1–4.
- [29] Y. Ichikawa, R. Tokoro, M. Tanno, K. Ogawa, Elucidation of cold-spray deposition mechanism by auger electron spectroscopic evaluation of bonding interface oxide film, *Acta Mater.* 164 (2019) 39–49.
- [30] H. Assadi, F. Gärtner, T. Stoltzenhoff, H. Kreye, Bonding mechanism in cold gas spraying, *Acta Mater.* 51 (2003) 4379–4394.
- [31] J.Y. Lek, A. Bhowmik, A.W. Tan, W. Sun, X. Song, W. Zhai, P.J. Buenconsejo, F. Li, E. Liu, Y.M. Lam, C.K. Boothroyd, Understanding the microstructural evolution of cold sprayed Ti-6Al-4V coatings on Ti-6Al-4V substrates, *Appl. Surf. Sci.* 459 (2018) 492–504.
- [32] M. Hassani-Gangaraj, D. Veysset, V.K. Champagne, K.A. Nelson, C.A. Schuh, Adiabatic shear instability is not necessary for adhesion in cold spray, *Acta Mater.* 158 (2018) 430–439.
- [33] S. Suresh, S.W. Lee, M. Aindow, H.D. Brody, V.K. Champagne, A.M. Dongare, Mesoscale modeling of jet initiation behavior and microstructural evolution during cold spray single particle impact, *Acta Mater.* 182 (2020) 197–206.
- [34] S. Yin, J. Cizek, J. Cupera, M. Hassani, X. Luo, R. Jenkins, Y. Xie, W. Li, R. Lupoi, Formation conditions of vortex-like intermixing interfaces in cold spray, *Mater. Des.* 200 (2021), 109444.
- [35] H. Assadi, F. Gärtner, T. Klassen, H. Kreye, Comment on ‘Adiabatic shear instability is not necessary for adhesion in cold spray’, *Scr. Mater.* 162 (2019) 512–514.
- [36] M. Hassani-Gangaraj, D. Veysset, V.K. Champagne, K.A. Nelson, C.A. Schuh, Response to Comment on ‘Adiabatic shear instability is not necessary for adhesion in cold spray’, *Scr. Mater.* 162 (2019) 515–519.
- [37] M. Hassani-Gangaraj, D. Veysset, K.A. Nelson, C.A. Schuh, In-situ observations of single micro-particle impact bonding, *Scr. Mater.* 145 (2018) 9–13.
- [38] M. Hassani-Gangaraj, D. Veysset, K.A. Nelson, C.A. Schuh, Melt-driven erosion in microparticle impact, *Nat. Commun.* 9 (2018) 1–7.
- [39] C.Y. Gao, L.C. Zhang, Constitutive modelling of plasticity of fcc metals under extremely high strain rates, *Int. J. Plast.* 32 (2012) 121–133.
- [40] S. Rahmati, A. Ghaei, The use of particle/substrate material models in simulation of cold-gas dynamic-spray process, *J. Therm. Spray. Technol.* 23 (2014) 530–540.
- [41] V. Lemiale, P.C. King, M. Rudman, M. Prakash, P.W. Cleary, M.Z. Jahedi, S. Gulizia, Temperature and strain rate effects in cold spray investigated by smoothed particle hydrodynamics, *Surf. Coat. Technol.* 254 (2014) 121–130.
- [42] W. Rae, Thermo-metall-mechanical modelling of heat treatment induced residual stress in Ti-6Al-4V alloy, *Mater. Sci. Technol.* 35 (2019) 747–766.
- [43] A. Rudnytskyj, P. Simon, M. Jech, C. Gachot, Constitutive modelling of the 6061 aluminium alloy under hot rolling conditions and large strain ranges, *Mater. Des.* 190 (2020), 108568.
- [44] A. Alizadeh-Dehkhanghani, Tuning Johnson-Cook, material model parameters for impact of high velocity, micron scale aluminum particles. Master thesis, Northeastern University,, 2016.
- [45] W. Xie, A. Alizadeh-Dehkhanghani, Q. Chen, V.K. Champagne, X. Wang, A.T. Nardi, S. Kooi, S. Müftü, J.H. Lee, Dynamics and extreme plasticity of metallic microparticles in supersonic collisions, *Sci. Rep.* 7 (2017) 5073.
- [46] R. Chakrabarty, J. Song, A modified Johnson-Cook material model with strain gradient plasticity consideration for numerical simulation of cold spray process, *Surf. Coat. Technol.* 397 (2020), 125981.
- [47] Q. Wang, N. Ma, M. Takahashi, X. Luo, C. Li, Development of a material model for predicting extreme deformation and grain refinement during cold spraying, *Acta Mater.* 199 (2020) 326–339.
- [48] Q. Wang, N. Ma, X. Luo, C. Li, Capturing cold-spray bonding features of pure Cu from in situ deformation behavior using a high-accuracy material model, *Surf. Coat. Technol.* 413 (2021), 127087.
- [49] R. Drehmann, T. Grund, T. Lampke, B. Wielage, K. Manygoats, T. Schucknecht, D. Rafaja, Interface characterization and bonding mechanisms of cold gas-sprayed Al coatings on ceramic substrates, *J. Therm. Spray. Technol.* 24 (2015) 92–99.
- [50] T. Akatsu, G. Sasaki, N. Hosoda, T. Suga, Microstructure and strength of Al-sapphire interface by means of the surface activated bonding method, *J. Mater. Res.* 12 (1997) 852–856.
- [51] S.T. Oyinbo, T.C. Jen, Investigation of the process parameters and restitution coefficient of ductile materials during cold gas dynamic spray (CGDS) using finite element analysis, *Addit. Manuf.* 31 (2020), 100986.
- [52] A.A. Hemeda, C. Zhang, X.Y. Hu, D. Fukuda, D. Cote, I.M. Nault, A. Nardi, V. K. Champagne, Y. Ma, J.W. Palko, Particle-based simulation of cold spray: influence of oxide layer on impact process, *Addit. Manuf.* 37 (2021), 101517.
- [53] B. Yildirim, H. Yang, A. Gouldstone, S. Müftü, Rebound mechanics of micrometre-scale, spherical particles in high-velocity impacts, *Proc. R. Soc. A-Math. Phys. Eng. Sci.* 473 (2017) 20160936.
- [54] G.I. Kanel, V.E. Fortov, S.V. Razorenov, Shock waves in condensed-state physics, *Phys. Usp.* 50 (2007) 771.
- [55] P.J. Wolcott, A. Hehr, M.J. Dapino, Optimized welding parameters for Al 6061 ultrasonic additive manufactured structures, *J. Mater. Res.* 29 (2014) 2055–2065.
- [56] S. Yadav, D.R. Chichili, K.T. Ramesh, The mechanical response of a 6061-T6 Al/ Al_2O_3 metal matrix composite at high rates of deformation, *Acta Metall. Et. Mater.* 43 (1995) 4453–4464.
- [57] E.B. Zaretsky, G.I. Kanel, Effect of temperature, strain, and strain rate on the flow stress of aluminum under shock-wave compression, *J. Appl. Phys.* 112 (2012), 073504.
- [58] B. Gurrutxaga-Lerma, M.A. Shehadeh, D.S. Balint, D. Dini, L. Chen, D.E. Eakins, The effect of temperature on the elastic precursor decay in shock loaded FCC aluminium and BCC iron, *Int. J. Plast.* 96 (2017) 135–155.
- [59] Z. Zhou, A.S. Gill, D. Qian, S.R. Mannava, K. Langer, Y. Wen, V.K. Vasudevan, A finite element study of thermal relaxation of residual stress in laser shock peened IN718 superalloy, *Int. J. Impact Eng.* 38 (2011) 590–596.
- [60] M. Daoud, J.F. Chatelain, A. Bouzid, Effect of rake angle-based Johnson-Cook material constants on the prediction of residual stresses and temperatures induced in Al2024-T3 machining, *Int. J. Mech. Sci.* 122 (2017) 392–404.
- [61] I.A. Bataev, S. Tanaka, Q. Zhou, D.V. Lazurenko, A.J. Junior, A.A. Bataev, K. Hokamoto, A. Mori, P. Chen, Towards better understanding of explosive welding by combination of numerical simulation and experimental study, *Mater. Des.* 169 (2019), 107649.
- [62] R.L. Doney, J.H. Niederhaus, T.J. Fuller, M.J. Coppinger, Effects of equations of state and constitutive models on simulating copper shaped charge jets in ALEGRA, *Int. J. Impact Eng.* 136 (2020), 103428.